Fe/Fe_3O_4 Heterostructures Supported on N, O-Doped Hollow Carbon Spheres with High Catalytic Performance for Oxygen Reduction and Zinc-Air Batteries

Chen-Yu Song†, Chen-Jin Huang†, Hong-Cheng Zhang, Hui-Min Xu, Shao-Lan zheng, Ruo-Zheng Xiong, Gao-Ren Li*

College of Materials Science and Engineering, Sichuan University, Chengdu 610065, China

E-mail: ligaoren@scu.edu.cn

†These authors contributed equally: Chen-Yu Song, Chen-Jin Huang

Methods and characterizations

1. Materials

All chemical reagents used in this study were of commercial grade. Ferric nitrate ($Fe(NO_3)_3 \cdot 9H_2O$), potassium hydroxide (KOH, 99.95 wt%) , 2-methylimidazole (AR), concentrated ammonia aqueous solution ($NH_3 \cdot H_2O$, 25%), tetraethyl silicate (TEOS), resorcinol, formaldehyde (37%), and ethanol (AR) were purchased from Shanghai Aladdin Reagent Co., Ltd. 40 wt% Pt/C was purchased from Suzhou Sino-Ro Technology Co., Ltd. Zinc nitrate hexahydrate ($Zn(NO_3)_2 \cdot 6H_2O$) was purchased from Chengdu Kron Chemical Co., Ltd. Deionized water was used throughout the experiment.

2. Synthesis of phenolic-based carbon microspheres

The synthesis method has been previously reported in the literature.[1] First, 2.88 mL of TEOS was added to a solution containing 55 mL of ethanol, 7 mL of water, and 2 mL of $NH_3 \cdot H_2O$ (25 wt%). After 30 minutes, 0.4 g of resorcinol and 0.56 mL of formaldehyde (37%) were added to the solution, which was then stirred at room temperature for 18 hours. The precipitate was then separated by centrifugation, washed three times with water and ethanol, and dried overnight at 60°C. Phenolic carbon microspheres were prepared by carbonizing the precipitate at 650°C under pure argon for 6 hours, followed by etching away the silica using hydrofluoric acid (HF, 6–7 wt%) under ultrasonic agitation for 30 minutes. The acid-etched waste solution was treated with calcium hydroxide solution and dried to yield black powder.

3. Synthesis of Fe/Fe_3O_4@NOC

In a typical synthesis of Fe/Fe_3O_4 loaded onto phenolic-based carbon microspheres, 40 mg of phenolic-based carbon microspheres and 0.41 g of 2-methylimidazole were dissolved in 20 mL of deionized water. The mixture was sonicated for 30 minutes to ensure uniform dispersion, and the resulting solution was designated as Solution A. 1.8

mmol of $Zn(NO_3)_2 \cdot 6H_2O$ and 0.05 mmol of $Fe(NO_3)_3 \cdot 9H_2O$ were dissolved in 5 mL of deionized water and sonicated for 5 minutes to ensure uniform dispersion within the solution; this was designated as Solution B. Solution B was then added dropwise to Solution A at a constant rate of 5 mL/min. The mixture was stirred at room temperature for 4 hours, then centrifuged to separate the precipitate, which was dried overnight in a vacuum oven at 60°C. The dried sample was ground and heated to 900°C at a heating rate of 5°C/min under an argon atmosphere for 3 hours, then cooled to ambient temperature (the sample is denoted as Fe/Fe_3O_4@NOC).

4. Synthesis of Fe_3O_4@NOC

Dissolve 1.2 mmol of $Zn(NO_3)_2 \cdot 6H_2O$ and 0.05 mmol of $Fe(NO_3)_3 \cdot 9H_2O$ in 5 mL of deionized water, and sonicate for 5 minutes to ensure uniform dispersion within the solution; this is designated as Solution C. Subsequently, Solution C is added dropwise to Solution A at a constant rate of 5 mL/min. After stirring at room temperature for 4 hours, the precipitate was separated by centrifugation and dried overnight in a vacuum oven at 60°C. The dried sample was ground and then heated to 900°C at a heating rate of 5°C/min under an argon atmosphere for 3 hours, followed by cooling to ambient temperature (the sample is denoted as Fe_3O_4@NOC).

5. Synthesis of Fe@NOC

Solution C was added dropwise at a constant rate to solution A. Following the same procedure, the mixture was heated at a rate of 5°C/min to 900°C under a hydrogen-argon atmosphere for 3 hours, then cooled to room temperature (the sample is denoted as Fe@NOC).

6. Synthesis of NOC

Dissolve 1.2 mmol of $Zn(NO_3)_2 \cdot 6H_2O$ in 5 mL of deionized water and sonicate for 5 minutes to ensure uniform dispersion within the solution; this solution is designated as Solution D. Following the same procedure, heat the solution in a hydrogen atmosphere at a rate of 5 °C/min until it reaches 900 °C, maintain this temperature for 3 hours, and then cool to room temperature (the sample is designated as NOC).

7. Materials characterizations

A scanning electron microscope (SEM, Thermo Fisher Quattro S) was used to characterize the morphological structure and microstructure of the samples. A high-resolution transmission electron microscope (HRTEM) and a transmission electron microscope (TEM) were used to analyze the microstructural details and elemental distribution of the materials. An X-ray diffractometer (XRD) (Bruker D8) was used to determine the form of the samples and their crystal structures. A Micromeritics ASAP 2460 was used to evaluate the pore size distribution and specific surface area of the samples. X-ray photoelectron spectroscopy (XPS, Thermo Scientific K-Alpha) was employed to analyze the surface chemical composition of the samples. Raman spectra of the samples were acquired using a HORIBA

XploRA Plus under ambient conditions with a 532 nm laser source.

8. Electrochemical measurements

5 mg of catalyst in a solution prepared from 20 μl of 5 wt% Nafion, 800 μl of ethanol, and 180 μl of deionized water was dissolved to form a uniformly dispersed ink. A 40 μl drop of the ink was dispensed onto a 0.196 cm^2 glassy carbon electrode to serve as the working electrode. The catalyst and Pt/C were loaded at a loading of 1 mg cm^{-2}. A graphite rod and a Hg/HgO electrode were selected as the counter electrode and reference electrode, respectively. A standard three-electrode cell was then set up in a 0.1 M KOH electrolyte for ORR testing.

The ORR catalytic activity of the catalyst was measured using the CHI660E electrochemical workstation. First, bring the electrolyte to a state of oxygen saturation, and maintain this state by continuously bubbling gas throughout the electrochemical test. Calibrate all potentials using a reversible hydrogen electrode (RHE) according to the following equation:

$$E_{RHE} = E_{Hg/HgO} + 0.0592\text{pH} + 0.098\ \text{V} \qquad (1)$$

The catalyst was activated within the reaction potential range, and linear sweep voltammetry (LSV) was performed on a rotating disk electrode at speeds ranging from 400 to 2025 rpm. The Tafel slope was determined from the linear fit of potential versus current density on a logarithmic scale. The ORR was studied using cyclic voltammetry (CV) in 0.1 M KOH electrolyte saturated with N_2 or O_2. At a rotation speed of 1600 rpm, the initial polarization curve was measured using an LSV test in O_2-saturated 0.1 M KOH at a scan rate of 10 mV/s within the voltage range of 0.2–1.2 V vs. RHE. The polarization curve was measured again after 5000 cycles to evaluate the decay of the half-wave potential and verify durability and stability. Electrochemical impedance spectroscopy (EIS) was performed in 0.1 M KOH electrolyte at open-circuit voltage, with a frequency window of 10^6 to 10^{-2} Hz and an amplitude of 5 mV. At a potential of 0.4 V vs. RHE, the change in current before and after the addition of methanol was recorded to evaluate methanol tolerance. The electrochemical active surface area (ECSA) can be indirectly represented by the double-layer capacitance (C_{dl}). Within the non-Faradaic potential range (e.g., 0.15–0.25 V vs. Hg/HgO), a series of CV measurements were performed at scan rates of 2, 4, 6, 8, and 10 mV/s. The slope of the fitted line $(J_a–J_c)/2\nu$ was then calculated, and this value represents the double-layer capacitance C_{dl}. Here, C_{dl} is the electrochemical double-layer capacitance, ν is the scan rate, J_a is the forward scan current density at the midpoint of the voltage range, and J_c is the reverse scan current density at the midpoint of the voltage range.

The electrochemical surface area (ECSA) of the material is calculated as $ECSA = C_{dl}/C_s$, and the specific capacitance Cs value is approximately 0.04 mF cm^{-2}. [2-3]

Furthermore, the kinetic current density (J_K) and the number of electron transfers (n) of the catalyst were calculated using the Koutecky-Levich equation. The formula is as follows:

$$\frac{1}{J}=\frac{1}{J_L}+\frac{1}{J_K}=\frac{1}{Bw^{0.5}}+\frac{1}{J_K} \quad (2)$$

$$B = 0.62\, nFC_0(D_0)^{2/3}v^{-1/6} \quad (3)$$

The meaning of each parameter in the formula (2) is as follows: J represents the current density obtained in the actual test (multiple sets of data can be obtained by adjusting the rotating disk electrode speed). J_K and J_L represent current densities limited by kinetic and diffusion control, respectively. The value of B can be determined by fitting the slope obtained from the KL equation. In the formula, n represents the number of electron transfers. F stands for Faraday constant, which is 96,485 coulombs per mole. C_0 stands for oxygen concentration, which is 1.26×10^{-6} moles per cubic centimeter. D_0 represents the diffusion value of oxygen in 0.1 M KOH, which is 1.9×10^{-5} cm^2 s^{-1}. v represents the kinetic viscosity, which is equal to 0.01 cm^2 s^{-1}.

9. ZAB measurements

Battery performance was evaluated using a homemade ZAB. First, 5 mg of catalyst was dissolved in a solution consisting of 20 µl of 5 wt% Nafion, 800 µl of ethanol, and 180 µl of deionized water to form a uniformly dispersed ink. The ink was then evenly drop-coated onto carbon paper to ensure a catalyst loading of 1 mg cm^{-2} over a circular area of 0.5 cm^2. A porous membrane was used as the gas diffusion layer, and foamed nickel as the current collector layer. The three layers were laminated in the order of gas diffusion layer, current collector layer, and catalyst layer to form the air cathode, preventing liquid leakage caused by excessive gaps in the mold. Additionally, a 99.9% pure zinc foil measuring 34 mm in length, 85 mm in width, and 0.5 mm in thickness was used as the anode. A mixed solution of 0.2 mol/L zinc acetate and 6 mol/L KOH served as the electrolyte. The components are assembled into a zinc-air battery within the mold, ensuring that both the zinc electrode and the air cathode have a contact area of 0.5 cm^2 with the electrolyte, and the current is normalized based on this. The volume of the electrolyte chamber is 10 cm^3, and the chamber is kept filled with electrolyte throughout the testing process.

All tests were conducted at room temperature under ambient conditions. LSV testing of the ZAB was performed using a CHI660E electrochemical workstation at a scan rate of 10 mV/s. The discharge power density was calculated based on the LSV curve using the following formula (4):

$$P = J_d \times U_d \quad (4)$$

where P is the discharge power density, J_d is the discharge current density, and U_d is the discharge voltage.

The discharge capacity of ZAB is evaluated by constant-current discharge at 10 mA cm^{-2}, and the formula (5) for specific capacity is as follows:

Specific capacity (mAh g^{-1}) =I $\Delta t/W_{Zn}$ (5)

Here, I, V, Δt, and W_{Zn} represent current, average discharge voltage, test duration, and the amount of Zn consumed, respectively.

In the cycling test, 200 charge-discharge cycles (10 minutes + 10 minutes) were performed at a current density of 10 mA cm^{-2}.

10. Computational methods

All the calculations are performed in the framework of the density functional theory with the projector augmented plane-wave method, as implemented in the Vienna ab initio simulation package.[4] The generalzied gradient approximation proposed by Perdew, Burke, and Ernzerhof is selected for the exchange-correlation potential.[5] The long range van der Waals interaction is described by the DFT-D3 approach.[6] The cut-off energy for plane wave is set to 520 eV. The energy criterion is set to 10^{-4} eV in iterative solution of the Kohn-Sham equation. The Brillouin zone integration is performed using a k-mesh grid with a density of 0.04 2π/Å. All the structures are relaxed until the residual forces on the atoms have declined to less than 0.03 eV/Å.

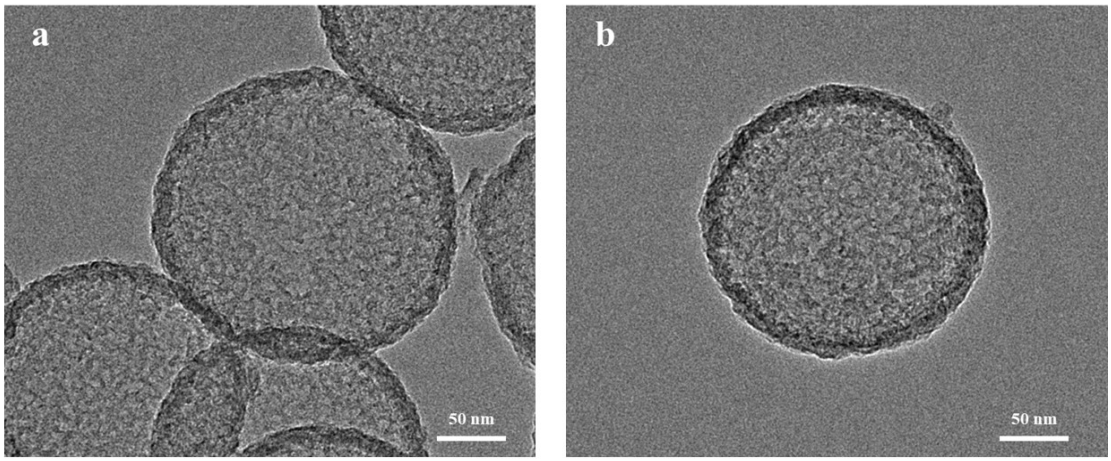

Figure S1. TEM images of phenolic hollow carbon spheres.

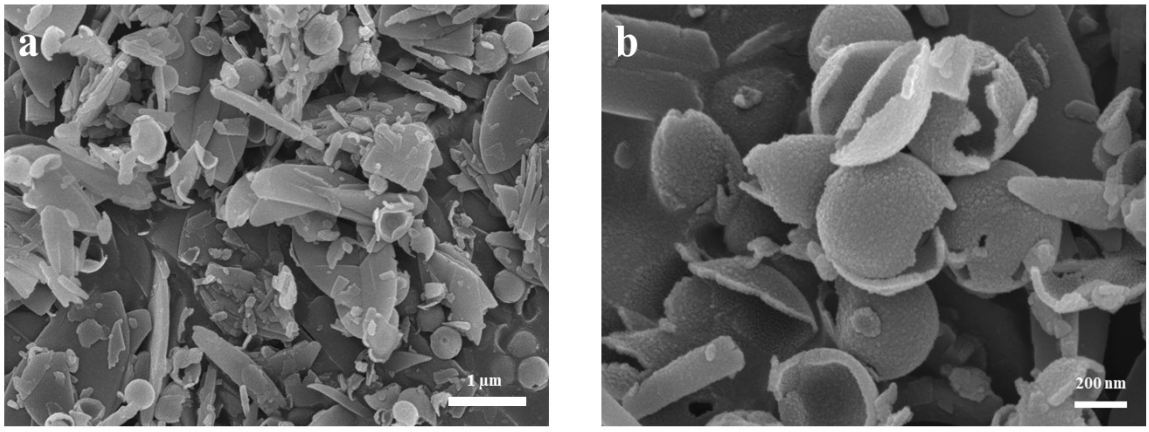

Figure S2. SEM images of Fe_3O_4@NOC and Fe@NOC precursors (n_{Zn}=1.2 mmol) with different magnifications.

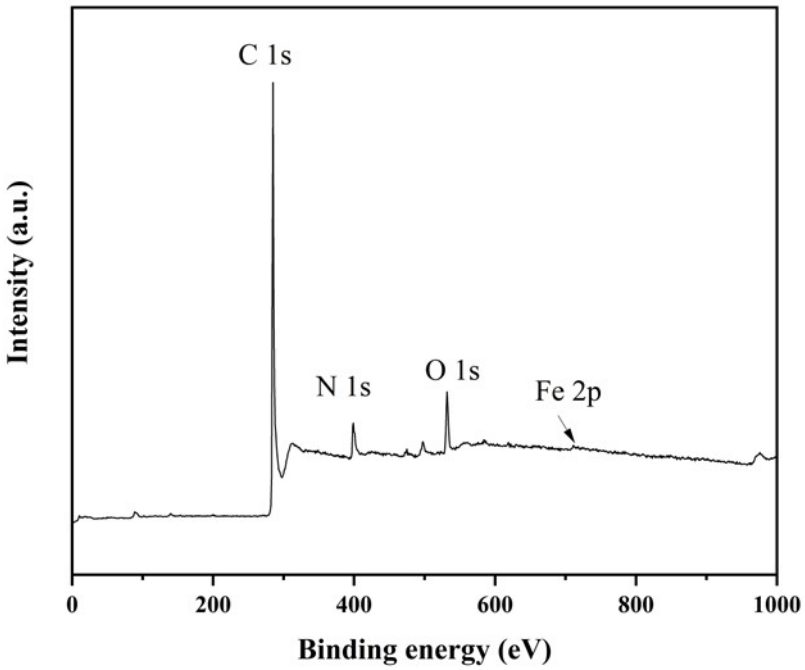

Figure S3. Full XPS spectrum of Fe/Fe_3O_4@NOC.

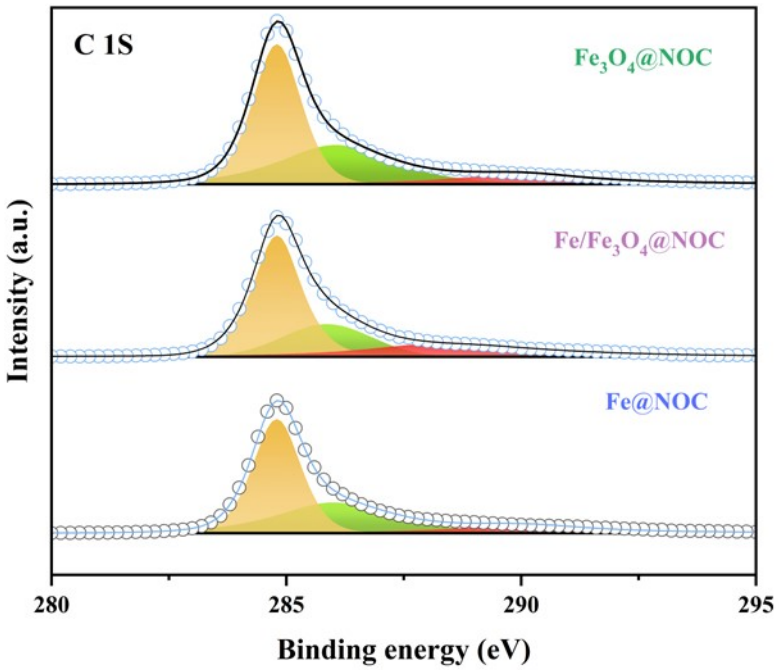

Figure S4. High-resolution C 1s XPS spectra of Fe_3O_4@NOC, Fe @NOC, and Fe/Fe_3O_4@NOC

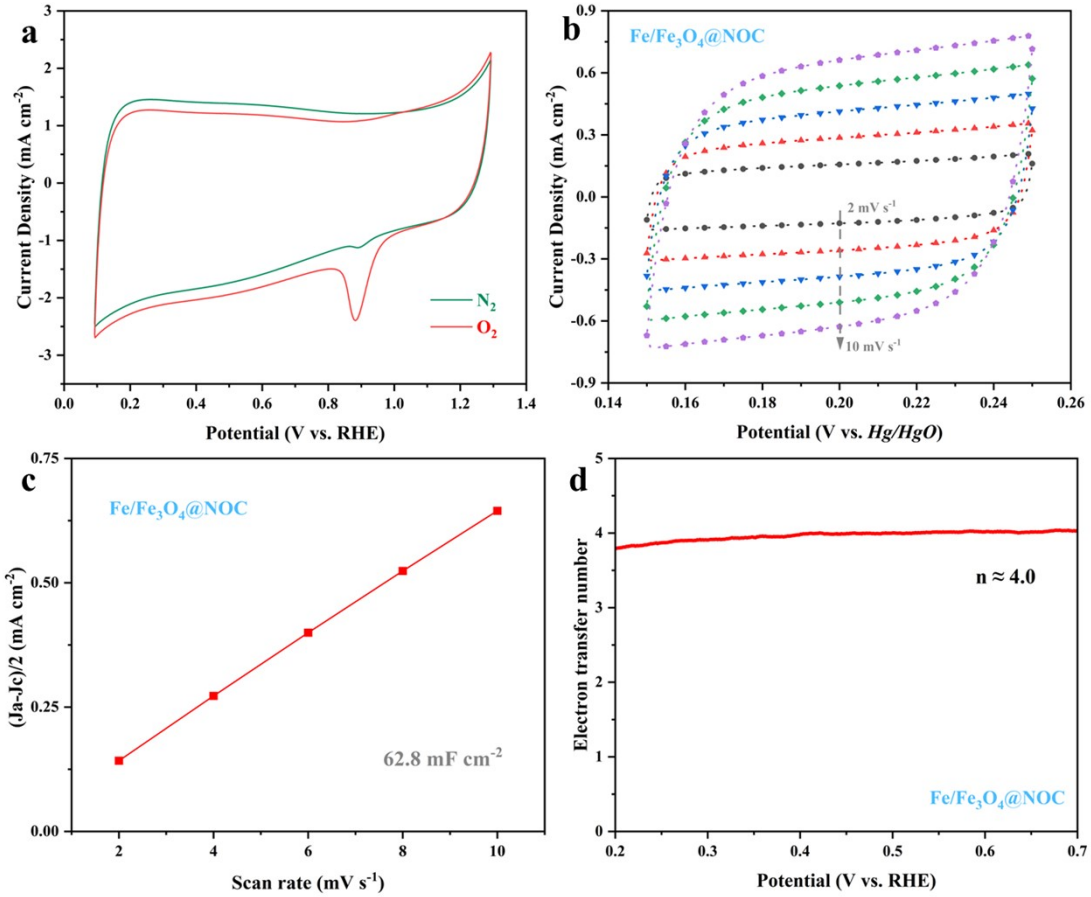

Figure S5. (a) CV curves of Fe/Fe_3O_4@NOC in O_2-saturated 0.1 M KOH solution and in N_2-saturated 0.1 M KOH solution; (b) CV curves of Fe/Fe_3O_4@NOC at scan rates of 2, 4, 6, 8, and 10 mV s^{-1} in 0.1 M KOH solution; (c) The capacitive current density as a function of scan rate at 0.10 V for Fe/Fe_3O_4@NOC catalysts; (d) Electron transfer number of Fe/Fe_3O_4@NOC.

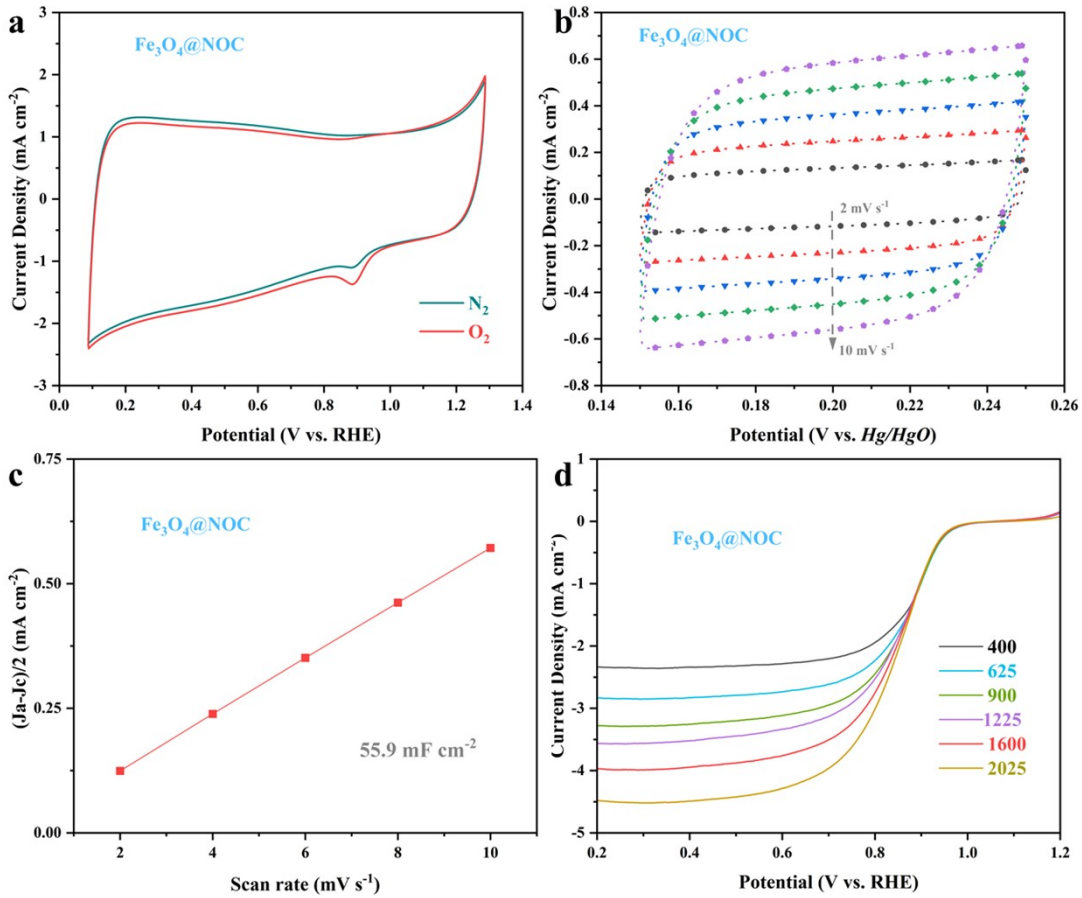

Figure S6. (a) CV curves of Fe_3O_4@NOC in O_2-saturated 0.1 M KOH solution and in N_2-saturated 0.1 M KOH solution; (b) CV curves of Fe_3O_4@NOC at scan rates of 2, 4, 6, 8, and 10 mV s^{-1} in 0.1 M KOH solution; (c) The capacitive current density as a function of scan rate at 0.10 V for Fe_3O_4@NOC catalysts; (d) LSVs of Fe_3O_4@NOC at different rotation speeds from 400 rpm to 2025 rpm.

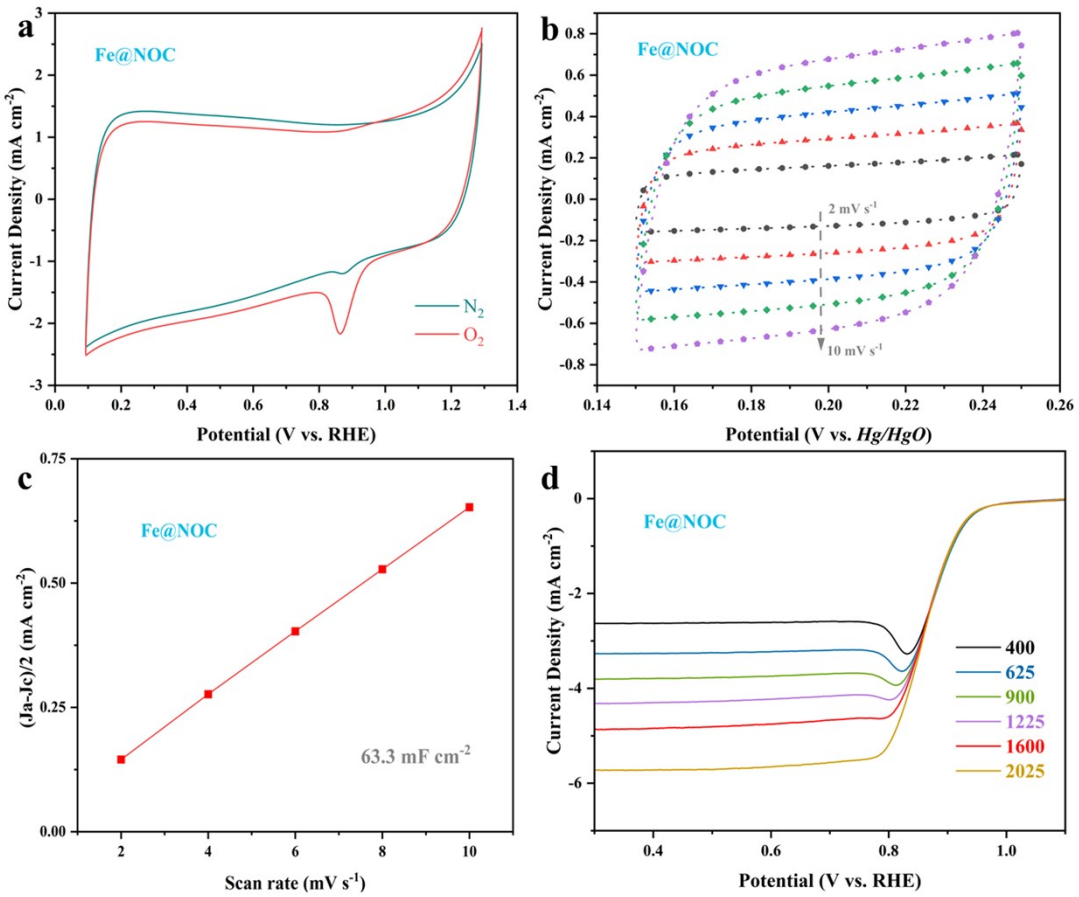

Figure S7. (a) CV curves of Fe@NOC in O_2-saturated 0.1 M KOH solution and in N_2-saturated 0.1 M KOH solution; (b) CV curves of Fe@NOC at scan rates of 2, 4, 6, 8, and 10 mV s^{-1} in 0.1 M KOH solution; (c) The capacitive current density as a function of scan rate at 0.10 V for Fe@NOC catalysts; (d) LSVs of Fe@NOC at different rotation speeds from 400 rpm to 2025 rpm.

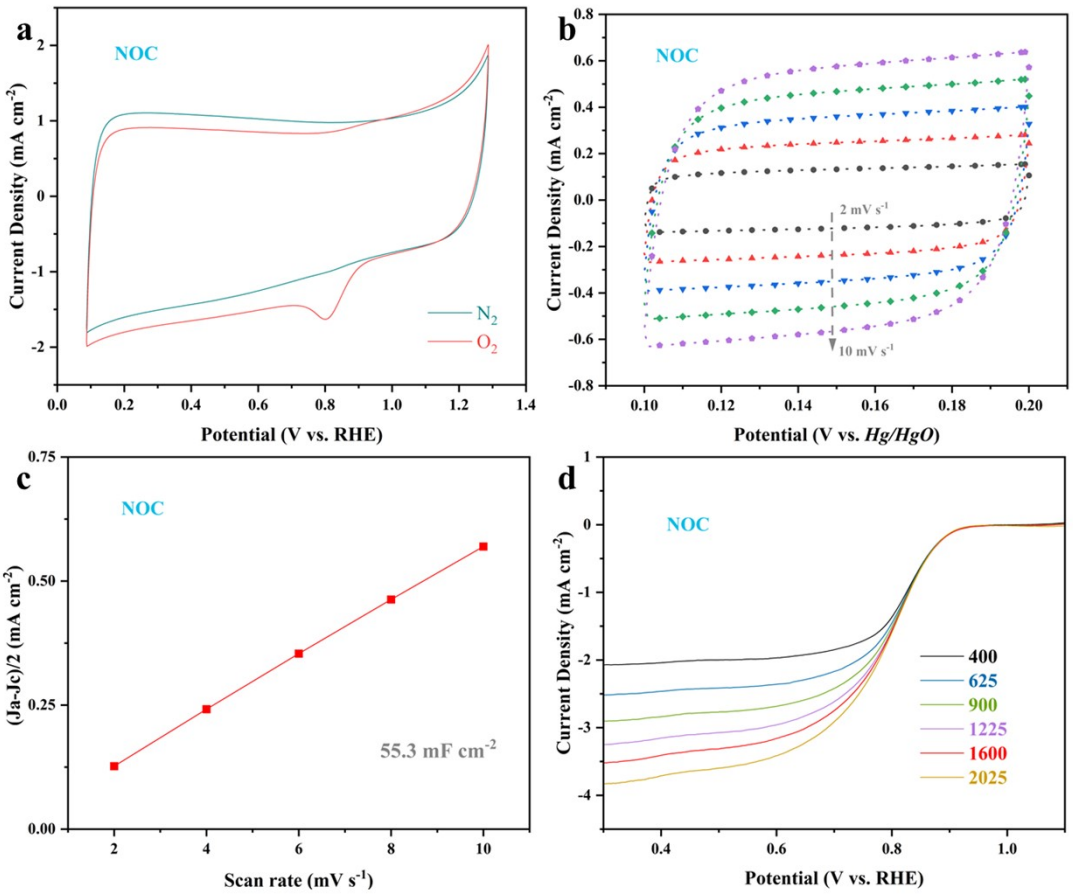

Figure S8. (a) CV curves of NOC in O_2-saturated 0.1 M KOH solution and in N_2-saturated 0.1 M KOH solution; (b) CV curves of NOC at scan rates of 2, 4, 6, 8, and 10 mV s^{-1} in 0.1 M KOH solution; (c) The capacitive current density as a function of scan rate at 0.10 V for NOC catalysts; (d) LSVs of NOC at different rotation speeds from 400 rpm to 2025 rpm.

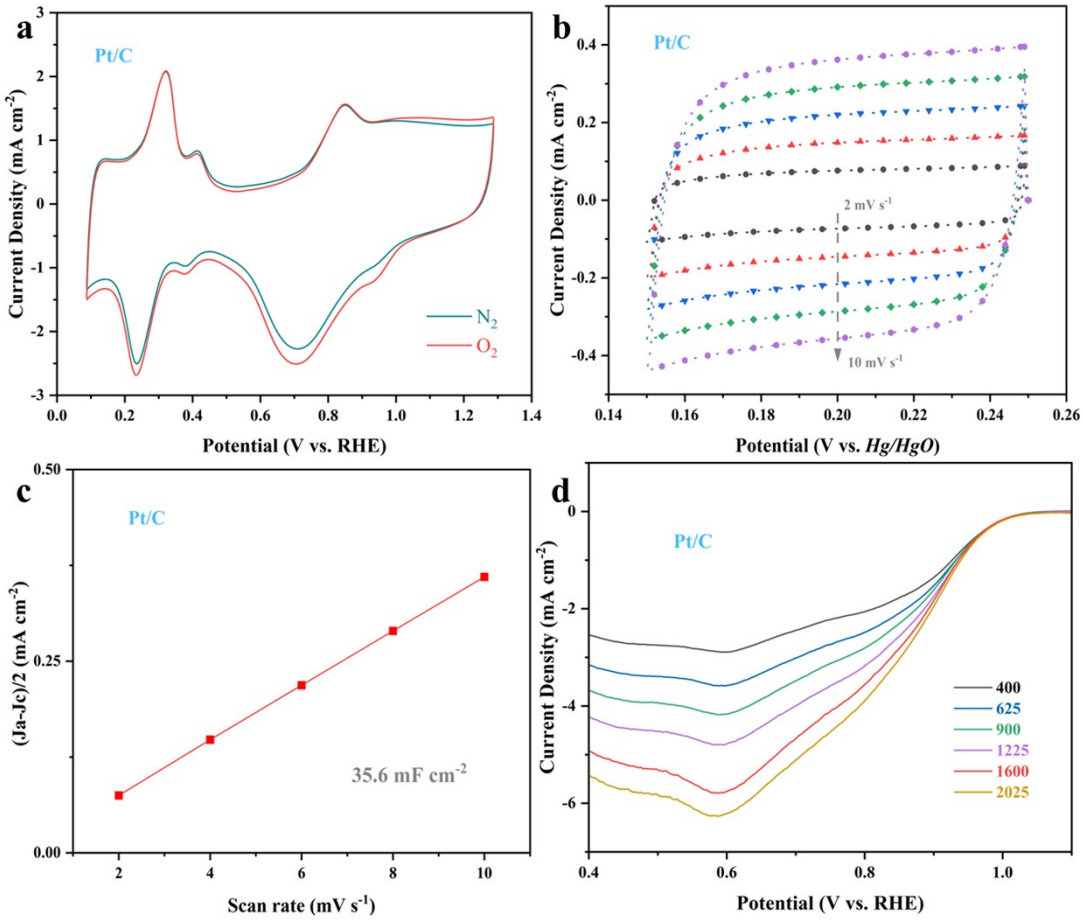

Figure S9. (a) CV curves of Pt/C in O_2-saturated 0.1 M KOH solution and in N_2-saturated 0.1 M KOH solution; (b) CV curves of Pt/C at scan rates of 2, 4, 6, 8, and 10 mV s^{-1} in 0.1 M KOH solution; (c) The capacitive current density as a function of scan rate at 0.10 V for Pt/C catalysts; (d) LSVs of Pt/C at different rotation speeds from 400 rpm to 2025 rpm.

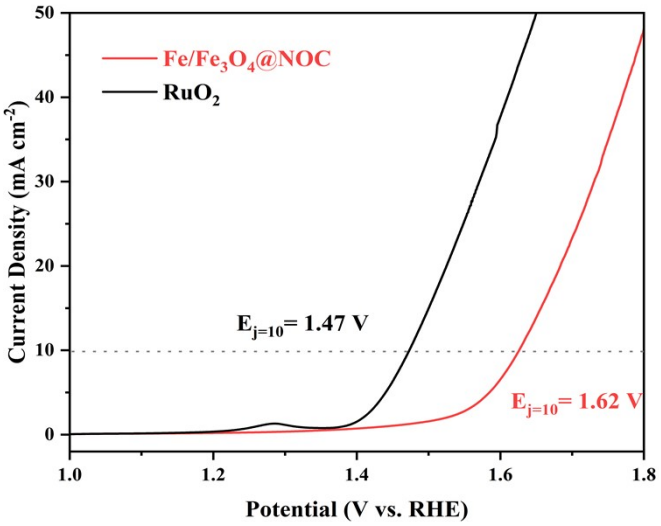

Figure S10. LSVs of OER on Fe/Fe_3O_4@NOC and RuO_2 in 1.0 M KOH electrolyte.

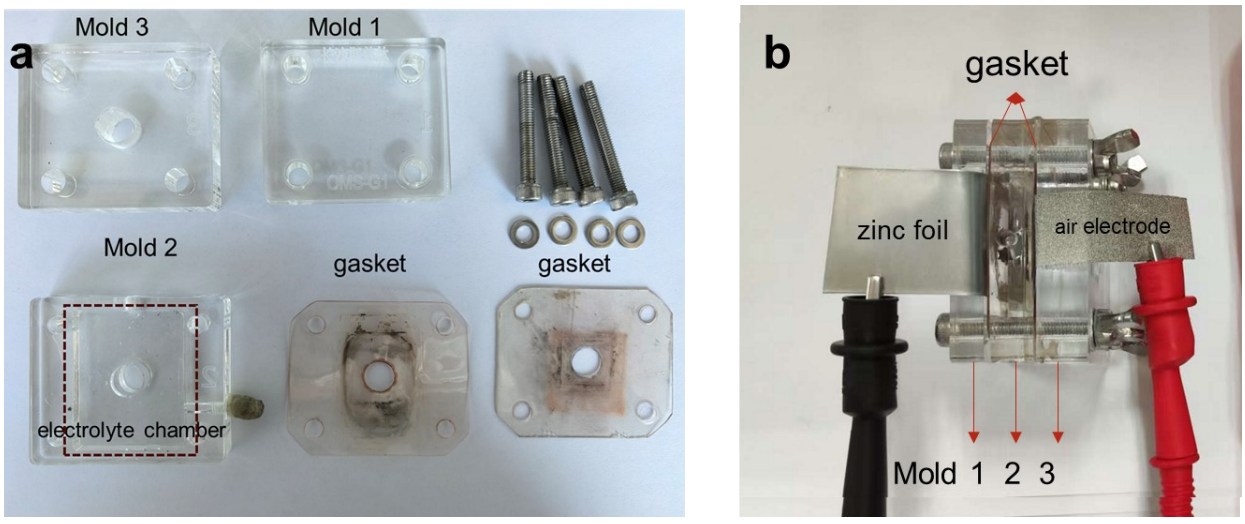

Figure S11. (a) Detailed Component Diagram of the ZAB Mold; (b) Assembly diagram of the ZAB.

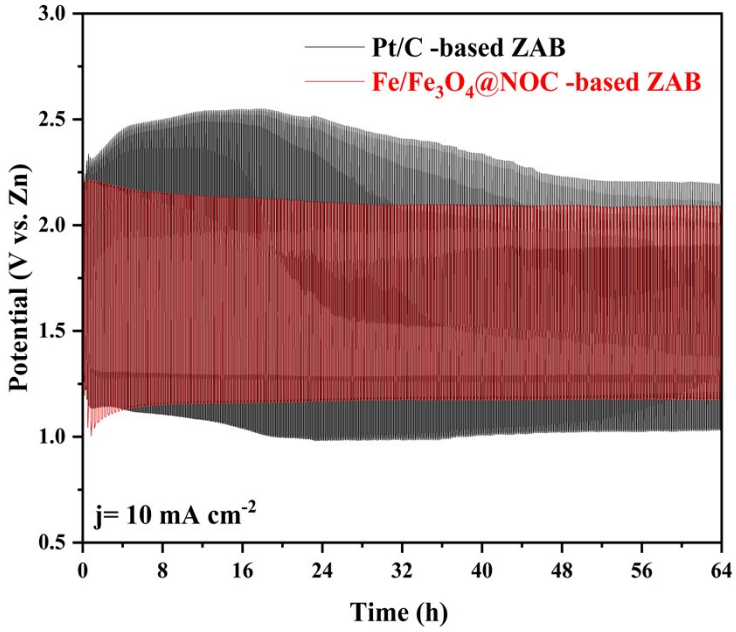

Figure S12. Long-term constant-current discharge-charge cycling curve of the Fe/Fe_3O_4@NOC-based ZAB and Pt/C- based ZAB at a current density of 10 mA cm^{-2}.

Table S1. Comparison of ORR activity of Fe/Fe_3O_4@NOC with previously reported non precious metal electrocatalysts.

Number	Catalyst	Load capacity (mg/cm^2)	Scan rate (mV/s)	Electrolyte	$E_{1/2}$/V	Stability	Ref
1	Fe/Fe_3O_4@NOC	1	10	0.1 M KOH	0.89	5 mV lost after 5000 cycles	This work
2	Fe SA/NSC-vd	N/A	10	0.1M KOH	0.92	Almost no attenuation after 10000 cycles	7
3	FeSA-Fe_3C/NC	0.4	10	0.1 M KOH	0.90	98.3% current remains After 43200 seconds	8
4	Co_3-NG	0.14	N/A	0.1 M KOH	0.90	93.8% current remains after 17h	9
5	FePc-Cl-CNTs	0.37	5	0.1 M KOH	0.91	15% current loss after 65000 s	10
6	Fe_2P@FeN_3P_1-NC	0.6	5	0.1 M KOH	0.88	86% current remains after 20000 seconds	11
7	CoNP/CoN_2-C	0.3	5	0.1 M KOH	0.89	37% current loss after 40000 s	12
8	CoCB	N/A	N/A	0.1 M KOH	0.87	93.9% current remains after 500h	13
9	Fe_1V_1-NC	0.42	10	0.1 M KOH	0.89	16 mV lost after 50000 cycles	14
10	HCHDC	0.6	10	0.1 M KOH	0.88	3 mV lost after 5000 cycles	15

Table S2. Comparison of the ZAB performance of Fe/Fe_3O_4@NOC with that of previously reported non-precious metal electrocatalysts in the same electrolyte.

Catalyst	Load capacity (mg/cm^2)	$E_{1/2}$/ V	$E_{j=10}$ /V	ΔE/ V	OCV /V	P_{max}/ mW cm^{-2}	Specific capacity/ mAh g_{Zn}^{-1}	Stability/ Duration (h)@j (mA cm^{-2})	Ref
Fe/Fe_3O_4@NOC	1	0.89	1.62	0.73	1.51	245.6	789.3	64@10	This work
FePc-Cl-CNTs	1	0.91	N/A	N/A	1.51	183.5	797.2	150@5	10
Fe_2P@FeN_3P_1-NC	2	0.88	1.55	0.67	1.50	227.3	N/A	37.5@7.8	11
FeSA-Fe_3C/NC	N/A	0.90	N/A	N/A	1.57	151.3	N/A	250@10	8
FeNb/c-SNC	2	0.92	N/A	N/A	N/A	341.3	N/A	1000@5	16
Co-N-C@MoS_2	1	0.87	1.57	0.7	N/A	168.4	772	400@5	17
CoP/FeP@PCN	1	0.89	1.46	0.566	1.52	175.4	780	579@5	18
Fe_1V_1-NC	1	0.89	N/A	N/A	1.50	237	795.0	400@10	14
MoCoP–NPC	1	0.88	1.55	0.67	1.50	175.2	829.6	300@10	3

References

1. H. Xu, X. Yin, M. Zhu, M. Han, Z. Hou, X. Li, L. Zhang and L. Cheng, ACS Appl. Mater. Interfaces, 2017, 9, 6332-6341.

2. X. Sun, Q. Shao, Y. Pi, J. Guo and X. Huang, Journal of Materials Chemistry A, 2017, 5, 7769-7775.

3. S. Zhao, S. Ran, N. Shi, M. Liu, W. Sun, Y. Yu and Z. Zhu, Small, 2023, 19, 2302414.

4. G. Kresse and D. Joubert, Phys. Rev. B, 1999, 59, 1758-1775.

5. J. P. Perdew, K. Burke and M. Ernzerhof, Phys. Rev. Lett., 1996, 77, 3865-3868.

6. S. Grimme, J. Antony, S. Ehrlich and H. Krieg, J. Chem. Phys., 2010, 132, 154104.

7. Y. Zhao, H.-C. Chen, X. Ma, J. Li, Q. Yuan, P. Zhang, M. Wang, J. Li, M. Li, S. Wang, H. Guo, R. Hu, K.-H. Tu, W. Zhu, X. Li, X. Yang and Y. Pan, Advanced Materials, 2024, 36, 2308243.

8. C. Liu, R. Yang, J. Wang, B. Liu, X. Chang, P. Feng, X. Zhang, L. Zhong, X. Zhao, L. Niu, S. Gan, Y. Xi, M. Huang and H. Wang, Angewandte Chemie International Edition, 2025, 64, e202501266.

9. T. Tang, X. Xu, X. Bai, C. Hou, T. Gan, Z. Wang and J. Guan, Angewandte Chemie International Edition, 2025, 64, e202503019.

10. M. Liu, Y. Liu, X. Zhang, L. Li, X. Xue, M. Humayun, H. Yang, L. Sun, M. Bououdina, J. Zeng, D. Wang, R. Snyders, D. Wang, X. Wang and C. Wang, Angewandte Chemie International Edition, 2025, 64, e202504923.

11. E. Zhu, C. Shi, J. Yu, H. Jin, L. Zhou, X. Yang and M. Xu, Applied Catalysis B: Environment and Energy, 2024, 347, 123796.

12. M. Wang, J. L. Chen, S. L. Zhang, Y. Y. Sun, W. L. Kong, L. N. Geng, Y. Li, L. M. Dai, Z. T. Li and M. B. Wu, Adv. Funct. Mater., 2024, 34.

13. Z. Yuan, J. Li, Z. Fang, M. Yang, L. Zhong, C. Liu, J. Ma, Z. Zeng, D. Yu, X. Chen and L. Dai, Angew. Chem. Int. Ed., 2025, 64, e202503936.

14. L. Ran, Y. Zhang, W. Tong, L. Chen, M. Wang, H. Zhou, P. Farràs, S. Chen and X. Qiu, Angewandte Chemie International Edition, 2025, 64, e202514542.

15. X. Wang, C. Han, Y. Han, R. Huang, H. Sun, P. Guo, X. Liu, M. Huang, Y. Chen, H. Wu, J. Zhang, X. Yan, Z. Mao, A. Du, Y. Jia and L. Wang, Small, 2024, 20, 2401447.

16. R. Sui, B. Liu, C. Chen, X. Tan, C. He, D. Xin, B. Chen, Z. Xu, J. Li, W. Chen, Z. Zhuang, Z. Wang and C. Chen, Journal of the American Chemical Society, 2024, 146, 26442-26453.

17. C. Hua, D. Ye, C. Chen, C. Sun, J. Fang, L. Liu, H. Bai, Y. Tang, H. Zhao and J. Zhang, Small, 2025, 21, 2412696.

18. K. Chen, L. Wang, J. Long, F. Zhao and L. Kang, Chemical Engineering Journal, 2024, 496, 153820.